Journal of Cleaner Production 275 (2020) 123767

Contents lists available at ScienceDirect

Journal of Cleaner Production

journal homepage: www.elsevier.com/locate/jclepro

Optimizing local climate zones to mitigate urban heat island effect in human settlements

Jun Yang [a, c], Yichen Wang [b, *], Chunliang Xiu [a], Xiangming Xiao [d], Jianhong Xia (Cecilia)[e], Cui Jin [c]

[a] Jangho Architecture College, Northeastern University, Shenyang, 110169, China
[b] College of Resource Environment and Toursim, Captial Normal Unversity, Beijing, 100048, China
[c] Human Settlements Research Center, Liaoning Normal University, Dalian, 116029, China
[d] Department of Microbiology and Plant Biology, Center for Spatial Analysis, University of Oklahoma, Norman, OK, 73019, USA
[e] School of Earth and Planetary Sciences (EPS), Curtin University, Perth, 65630, Australia

A R T I C L E I N F O

Article history:
Received 31 October 2019
Received in revised form
26 June 2020
Accepted 14 August 2020
Available online 23 August 2020

Handling editor: Cecilia Maria Villas Bôas de Almeida.

Keywords:
Land surface temperature
Urban heat island
Human settlements
Population
Luojia1-01
Dalian city

A B S T R A C T

Rapid urbanization has caused radical changes in urban climates. As a result, issues related to urban thermal environments have become more prominent. Finding a balance between urban expansion and thermal environment quality is key to ensuring sustainable urban development. Taking Dalian City (China) as an example, we used multi-source datasets, including Luojia1-01 nighttime light imagery, Landsat-8, Sentinel-2, and building vector data, to analyze the thermal characteristics of different local climate zones (LCZs). Additionally, the LCZ combination mode with the lowest heat island effect intensity in the human settlements was also investigated. The results showed that the human settlements covered an area of 351.976 km^2, with 33.476% corresponding to building LCZs (LCZ1-10) and 66.524% to natural LCZs (LCZA-G). The different LCZs had different thermal environment characteristics, and the UHIA values for the building LCZs were significantly higher than those of the natural LCZs. Additionally, for the building LCZs, the UHIA values for compact building LCZs (LCZ 1−3) were also significantly higher than those for open and spare building LCZs. With the current settlement area and population size, the most appropriate LCZ layout model for the study area was LCZ5 + LCZ6 + (LCZ7+LCZ8+LCZA + LCZC + LCZD + LCZE + LCZG), which had areas 28.585, 57.170, 57.170, 28.585, 54.236, 54.236, and 54.236 km^2, respectively. This layout model had the smallest UHIA value (11.654 °C), and urban planning according to the above ratio can alleviate the UHI effect in different cities.

1. Introduction

Since the 20th century, China's rapid urbanization and development as a big industrialized country has led to a significant upward trend in average annual surface temperatures. Rapid urbanization has led to environmental problems, and the interaction of the negative impacts of urban thermal environments poses an ongoing threat to urban human settlements (Yang et al., 2014; Zhang et al., 2007). Impervious surfaces that have significantly replaced original and natural surfaces owing to urban expansion and increasing population density in cities have resulted in a persistent increase in overall urban heat emissions. Consequently, this has significantly changed the original urban energy balance regime (Rizwan et al., 2008; Tu et al., 2016; J. Yang et al., 2018a,b, 2017a,b), and has resulted in a phenomenon known as the urban heat island (UHI) effect, whereby urban interior temperatures are generally higher compared with those of countryside areas. This UHI effect is the epitome of the issues that are associated with the urban thermal environment. In the context of global warming (Mitchell et al., 2016), extreme heat waves and UHI interact and promote each other. This interaction exacerbates the negative effects of the UHIs, and results in higher health risks for urban residents, as well as higher building energy consumption and CO_2 emissions (Tong et al., 2017; Wu et al., 2012). Additionally, these occurrences negatively affect the sustainable development cities (Chen et al., 2020; Yang et al., 2020).

* Corresponding author. College of Resource Environment and Toursim, Captial Normal Unversity, Beijing, 100048, China.
E-mail addresses: yangjun8@mail.neu.edu.cn (J. Yang), y.c.wang_geo@foxmail.com (Y. Wang), xiucl@nenu.edu.cn (C. Xiu), xiangming.xiao@ou.edu (X. Xiao), c.xia@curtin.edu.au (J. Xia), cuijin@lnnu.edu.cn (C. Jin).

https://doi.org/10.1016/j.jclepro.2020.123767
0959-6526/

UHIs can be divided into four categories, namely, boundary-layer heat islands (BLHIs), canopy-layer heat islands (CLHIs), surface heat islands (SHIs), and subsurface heat islands (SBHIs) (Oke, 1976; Voogt and Oke, 2003; Zhan et al., 2014; Zhou et al., 2016). Land surface temperature (LST) is an important indicator when measuring the scale of SHIs, given that it controls near-surface energy balance and affects the surface heat distribution process, which exhibits the most significant effect on urban climates (Li et al., 2019). Owing to the combination of the UHI effect and extremely high-temperature weather, there has been a degradation of the thermal environment in urban human settlements, which has resulted in higher health risks to urban residents (Bao-Jie He, 2018). Previous studies on the heat island effect have been primarily focused on three aspects, i.e., the observation of the heat island effect, the analysis of the driving mechanism, and research on mitigation strategies. Alleviating the UHI effect in human settlements via the rational adjustment and configuration of landscapes is of great significance to urban thermal environment-related research and planning (Manteghi Golnoosh and Mostofa, 2020; Yin et al., 2018). Based on existing literature, the strategies that can be employed to mitigate existing UHI effects can be roughly divided into two categories. The first category includes strategies that seek to improve the internal ventilation of cities via the adjustment of urban form and the use of natural ventilation (Jhaldiyal et al., 2018; Wong et al., 2010; Yao et al., 2018), while the second category includes strategies that focus on the use of green spaces, water, and other landscapes that have a cooling effect based on a reasonable arrangement (Brans et al., 2018; Du et al., 2019; Fahmy et al., 2018; Yan et al., 2018).

The local climate zone (LCZ) is an effective approach by which UHIs and urban thermal environments can be investigated. It combines buildings and surfaces, and generates a classification system that is suitable for urban thermal environment-related research (Stewart and Oke, 2012). Auer (1978) performed one of the earliest studies on urban climate zones (UCZs). To improve the surface indicator system that was previously sensitive to the thermal environment, and provide an objective and standardized classification system for urban thermal environment research based on the UCZs, Stewart (Stewart et al., 2014; Stewart and Oke, 2012) divided a city into built and natural environments known as the LCZ, and reportedly, there is a significant correlation between LCZs and SHIs. Previous studies on LCZs have been primarily focused on LCZ mapping (Quan et al., 2017; Shi et al., 2018; Unger et al., 2014; Xu et al., 2017a; Zheng et al., 2018), LCZ modification (Kotharkar and Bagade, 2018; J. Wang et al., 2015a,b; Wang and Ouyang, 2017), and the determination of the temporal and spatial variations of the thermal environment characteristics in different LCZs (Beck et al., 2018; Geletič et al., 2018; Y. Wang et al., 2017b; X. Yang et al., 2018a,b, 2017a,b).

Finding the balance between the urban thermal environment and human activities is a key issue in the heat island effect mitigation strategy. Under the current urban scale (built-up zone scale and population scale), the reasonable combination of the distribution of LCZs can enhance the reduction of the UHI effect, which can provide a reference basis for urban scientific planning and management. Taking Dalian city as an example, multi-source data was used to extract human settlements, analyze the thermal environment characteristics of different LCZs within the human settlements, and propose the most suitable local climate zone layout model based on certain population and human settlement size limits. The results obtained could serve as data that can be used to support scientific and rational urban landscape planning and decision making so as to alleviate the UHI effect and improve the quality of the human living environment in cities.

2. Data and methods

2.1. Study area

The downtown area of Dalian City is located between 121.275° and 121.750° E and 38.813°–39.087° N. It consists of four administrative districts, including Zhongshan, Xigang, Shahekou, and Ganjingzi, which cover an area of 620 km^2 (Fig. 1). Based on 2018 data, Dalian City has a resident population of 2.06 million.

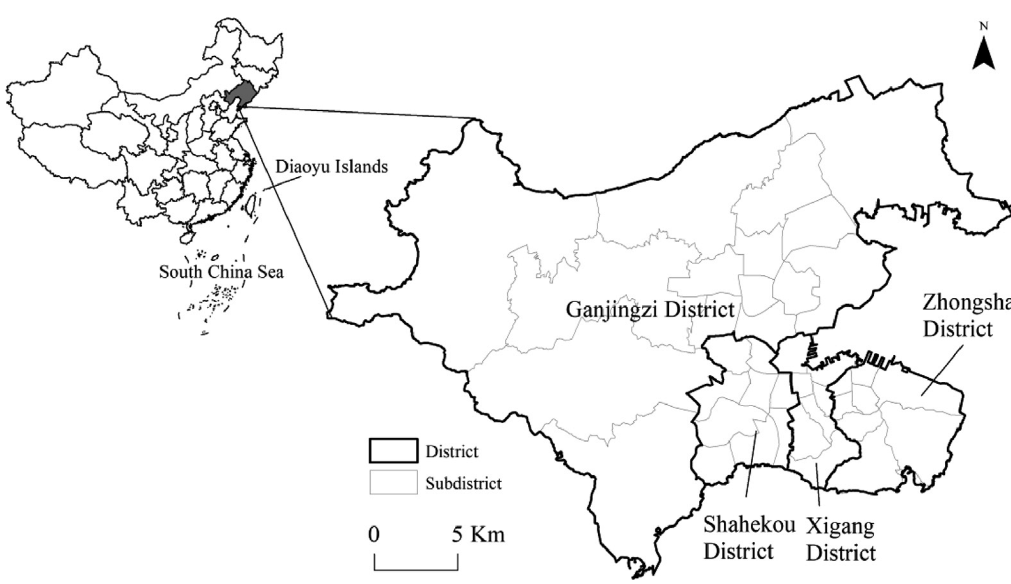

Fig. 1. The location of the study area.

Table 1
Data sources and descriptions.

Types	Description	Data sources	Display
Remote Sensing data	Luojia 1-01 (130-m resolution NTL data, 2018-9-9)	www.hbeos.org.cn	
	NPP-VIIRS (500-m resolution NTL data, 2018-9)	ngdc.noaa.gov/eog	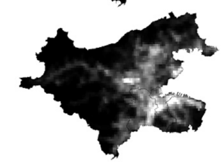
	DMSP/OLS F18 (1-km resolution NTL data, 2013)	ngdc.noaa.gov/eog	
	Sentinel-2 (10-m resolution multispectral, 2018-8-2, cloud cover: 0.1%)	Sci-Hub.copernicus.eu	
	Landsat8 TIRS (100-m resolution thermal, 2018-8-9, cloud cover: 0.4%) Landsat8 OLI (30-m resolution multispectral, 2018-8-9, cloud cover: 0.4%)	earthexplorer.usgs.gov	
	MODIS 11 L2 (1-km resolution LST product, 2018-8-9)	lpdaac.usgs.gov	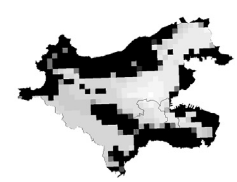
Meteorological data	Meteorological site observation data (air temperature and humidity data. From July 2018 to September 2018)	rp5.ru	
Building data	Building outline, height, floor and types.	Baidumap	
Population	Dalian Statistical Yearbook (2018)	Dalian Municipal Bureau of Statistics	–

2.2. Data sources

The main sources of the data used in this study included: remote sensing imagery, in-situ meteorological data, building vector data, and demographic data (Table 1). Fig. 2 shows the distribution of the building data.

2.3. Methods

2.3.1. LCZ mapping

The LCZs could be classified via the combination of urban surface properties and urban morphology using two main classification methods, namely, the direct interpretation of high-resolution imagery, such as the WUDAPT work fellow (He et al., 2018; Zheng et al., 2015), or integrated classification using multi-source data (Kotharkar and Bagade, 2018; Perera and Emmanuel, 2018). With Szeged (Hungary) as the study area, Gál et al. (2015) evaluated and compared the accuracy of these two methods. They found that integrated classification based on multi-source data had a higher accuracy than the direct interpretation of high-resolution imagery. Therefore, in this study, the LCZs of the study area were classified based on multi-source data via a classification process that could be divided into two steps as follows:

Fig. 2. Distribution of buildings in the study area.

Table 2
Local climate zone classification system.

Types	Description	Types	Description
LCZ1	Compact high-rise buildings	LCZA	Dense trees
LCZ2	Compact mid-rise buildings	LCZB	Scattered trees
LCZ3	Compact low-rise buildings	LCZC	Bush, scrub
LCZ4	Open high-rise buildings	LCZD	Low plants
LCZ5	Open mid-rise buildings	LCZE	Bare rock and road
LCZ6	Open low-rise buildings	LCZF	Bare soil
LCZ7	Spare high-rise buildings	LCZG	Water body
LCZ8	Spare mid-rise buildings		
LCZ9	Spare low-rise buildings		
LCZ10	Industrial buildings		

2.3.1.1. Nature zone classification. Nature zones were classified using the modified normalized difference water index (MNDWI) (Xu, 2006), normalized difference vegetation index (NDVI), the normalized difference impervious surface index (NDISI) (Xu, 2013), and the bare soil index (BSI) (Li and Chen, 2014). MNDWI was used to extract water bodies; NDVI and NDISI were used to distinguish vegetation and impervious surfaces, and BSI and NDVI were used to distinguish shrubs, low vegetation, and trees.

2.3.1.2. Building zone classification. Building zones were classified following building morphology. Even though numerous parameters are associated with the measurement of building morphology, in this study, two morphological indicators, building density (BD) and average building height (H), were selected to achieve objectivity and high efficiency (Yin et al., 2018).

2.3.1.3. LCZ classification system. Based on Oke et al. (2014) and Bechtel et al. (2016), we proposed a modified LCZ classification system (Table 2), which takes into account the actual building

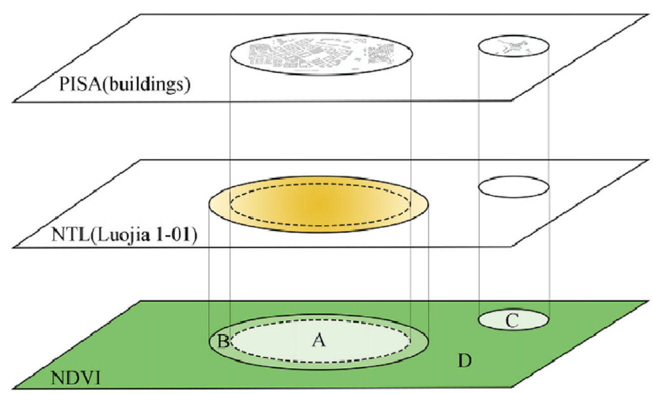

Fig. 3. HSCI in different areas.

distribution and land cover conditions of a specific study area. Making reference to previous studies on LCZ grid sizes, in this study a 30 m grid was used as the basic LCZ mapping unit (J. Yang et al., 2019a, 2019b).

2.3.2. Mapping of human settlements

There is a significant quantitative relationship between night-time light (NTL) radiation and several spatiotemporal parameters that are related to human population and socio-economics. To extract human settlements, previous studies have primarily relied on the extraction of impervious surfaces and the analyses of building aggregation patterns (Jochem et al., 2018; Maly, 2000). In several studies, artificial NTL data has often been used to estimate human activities that are related to urban expansion and socio-economic development (X. Yang et al., 2019; Ye et al., 2019). Urban NTL is a direct visual representation of the spatial

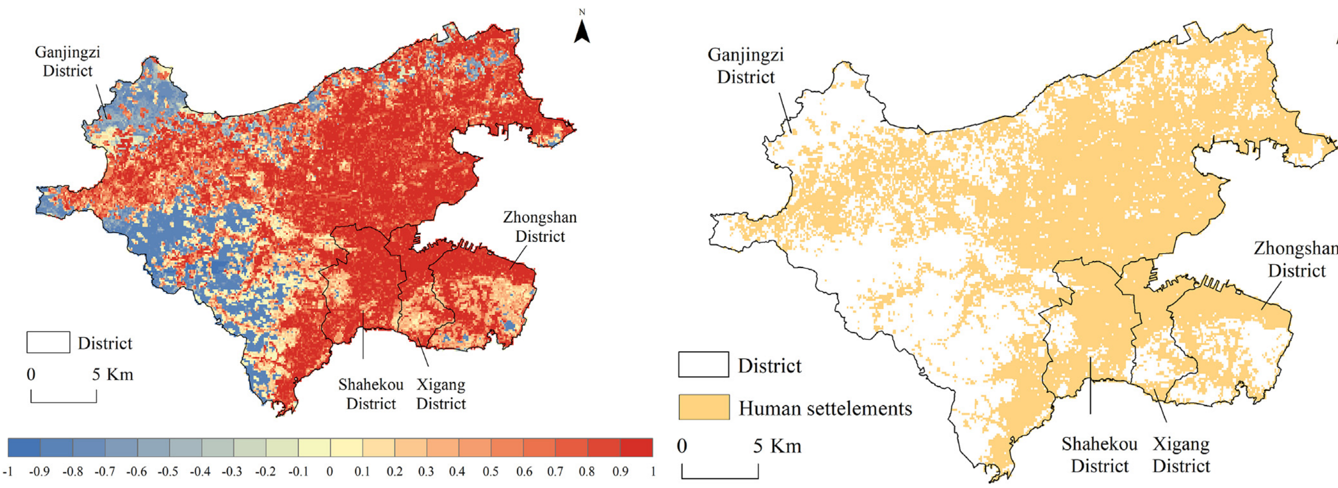

Fig. 4. Human settlements mapping results.

heterogeneity of urban human activity. Therefore, by combining multi-source data, such as remote sensing and land use data, it is possible to realize the efficient extraction of human settlements (Lu et al., 2008; Ma et al., 2018). Thus, NTL data is being increasingly used in the estimation of human activities that are related to urban expansion and socio-economic development. Using a combination of land cover and NTL data can lead to the efficient extraction of human settlements. Ma et al. (2018) proposed the human settlement composite index (HSCI), which combines vegetation, impervious surfaces, and NTL to realize the efficient extraction of human settlements. By combining the NDVI and the percentage impervious surface (PISA) with NTL data, the HSCI significantly improves accuracy when dividing human settlements. Additionally, it also reduces the effects of diffusion and saturation, while enhancing the heterogeneity of multi-source signals. The HSCI is calculated using the following equation:

$$\mathrm{HSCI} = \left(\mathrm{NTL} \times \mathrm{PISA} - \mathrm{NDVI}^2\right) / [(\mathrm{NTL} + \mathrm{NDVI})(\mathrm{PISA} + \mathrm{NDVI})]. \tag{1}$$

Fig. 3 illustrates the distribution of HSCI in different regions. Type A regions, where the HSCI tends towards 1, represent urban areas that are primarily characterized by strong brightness signals and impervious surfaces. Type B regions, where the HSCI is generally between 0 and 0.5 represent the areas surrounding cities, which have NTL signals, but no impervious surface. Type C regions, where the HSCI tends toward −0.5, represent rural areas with low human activity density, which have impervious surface coverage and has either no or low NTL signal. Type D regions represent areas with little human activity, where the HSIC trend to −1 and no NTL

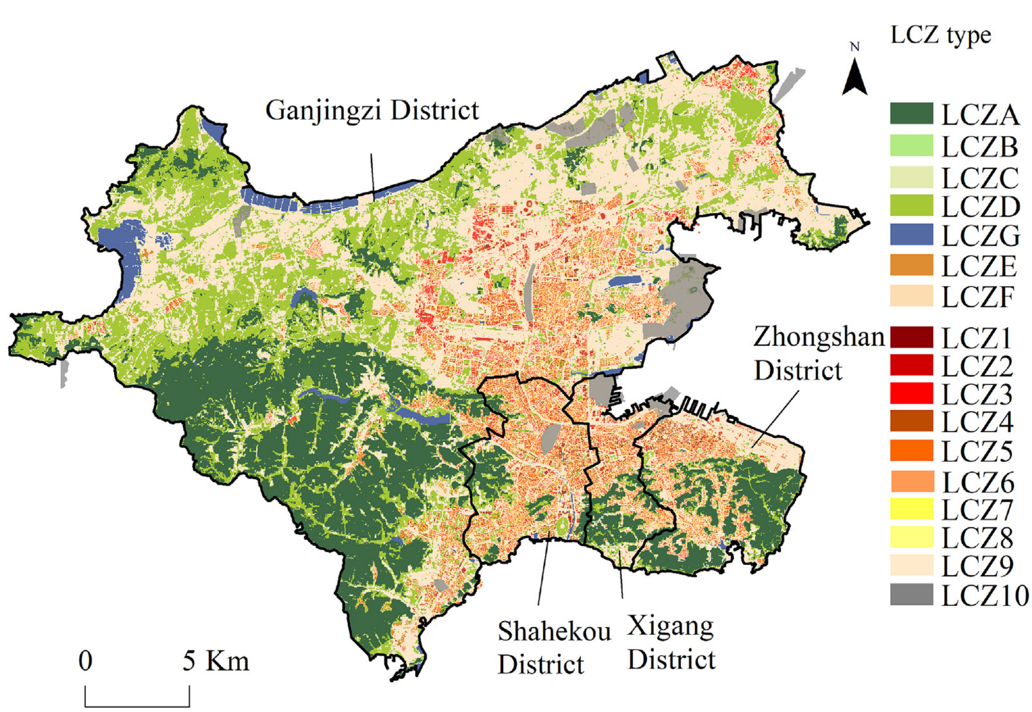

Fig. 5. LCZ mapping results.

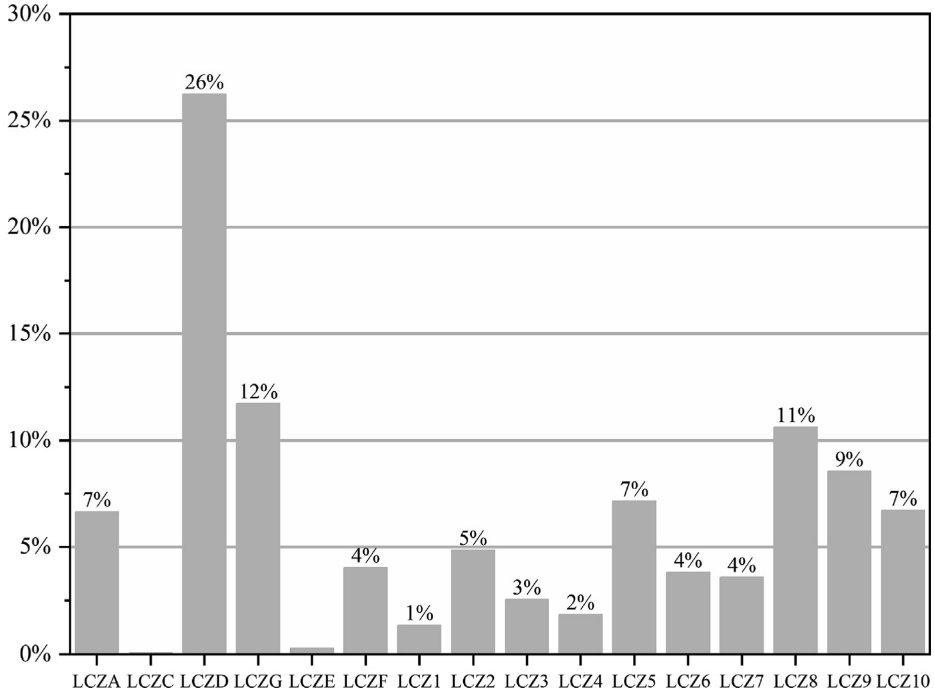

Fig. 6. The LCZ compositions in human settlements.

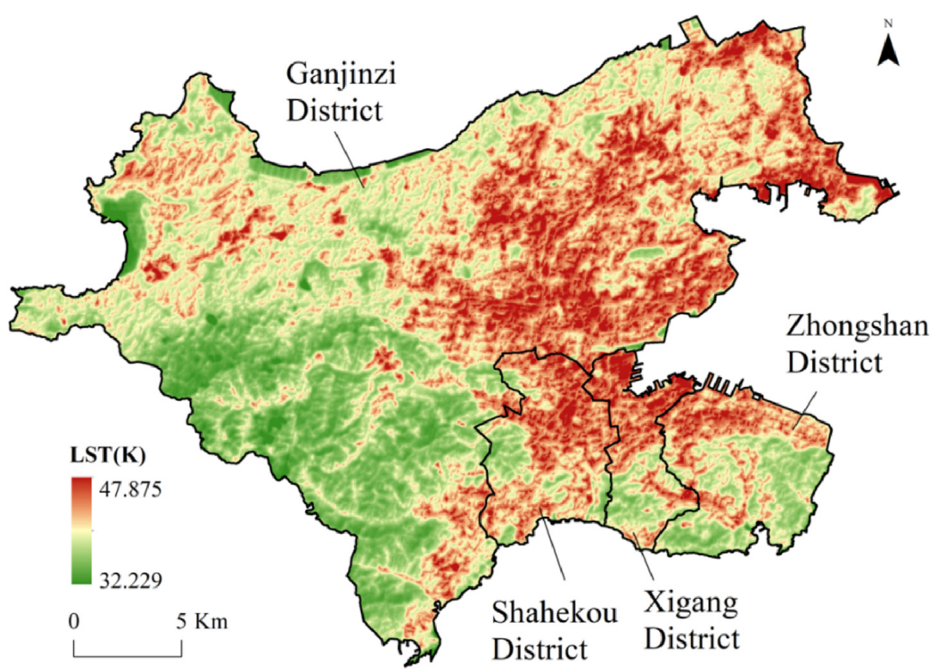

Fig. 7. Retrieved land surface temperatures.

signals or impervious surfaces. Compared with the DMSP/OLS data used when the HSCI was first proposed, Luojia 1-01 data is characterized by a higher spatiotemporal resolution without saturation effects (Jiang et al., 2018). Therefore, in this study, it was used to calculate the HSCI with a higher spatial resolution, offering the possibility of improving the precision of human settlement mapping.

2.3.3. LST inversion

In this study, Landsat8 band 10 and the mono-window algorithm were used to invert LST. The mono-window algorithm included various parameters, such as land surface emissivity (ε), atmospheric transmittance (τ), brightness temperature (T), and mean atmospheric temperature (T_a). LST was calculated using the following equations:

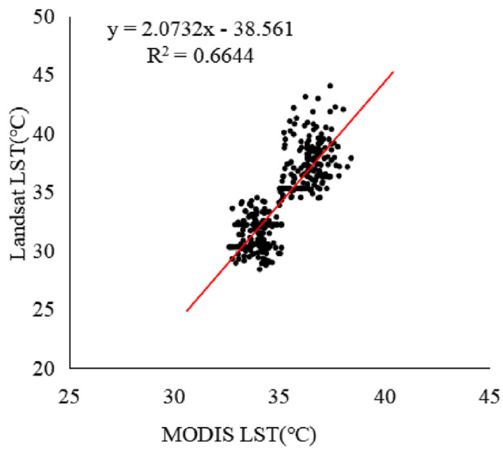

Fig. 8. Verification of the land surface temperature accuracy.

$$T_s = \{a*(1-C-D) + [b*(1-C-D) + C + D]T - D*T_a\}, \quad (2)$$

$$C = \tau*\varepsilon \quad (3)$$

$$D = (1-\tau)*[(1-\varepsilon)-\tau], \quad (4)$$

T_s (K) represents the LST, a and b are the fitting coefficients obtained from the relationship between the heat radiation intensity and the brightness temperature (i.e., when the latter was between 10 and 40 °C, a = −67.355351 and b = 0.458606), T represents the sensor brightness, and T_a (K) represents the average atmospheric operating temperature. The estimation of ε and τ were established according to Qin and Wang (Qin et al., 2001; F. Wang et al., 2015a,b).

3. Results

3.1. Human settlements and LCZ mapping

The HSCI values of the study area were calculated using Luojia 1-01 NTL image data at recorded 02:35 (GMT+8) on September 9, 2018, and Landsat 8 OLI image data recorded at 02:35 (GMT+8) on August 9, 2018. In accordance with Ma et al. (2018) areas with HSCI values above 0.65 were extracted as human settlements, as shown in Fig. 4.

The average HSCI value of the study area was 0.549, and the total human settlement area was 351.976 km^2. Additionally, the average HSCI values of each district, i.e., Zhongshan, Xigang, Shahekou, and Ganjingzi were 0.726, 0.861, 0.912, and 0.488, respectively, and the settlement area in each of these four administrative districts were 18.261, 28.454, 33.565, and 271.696 km^2, corresponding to 59.125%, 81.005%, 71.726%, and 55.570%, respectively.

The classification of the LCZs could be regarded as a combination of land cover and building morphology classifications. The LCZs, A–G were classified using the Sentinel-2 dataset and layer classification methods, after which the results obtained were then combined with the building classification results based on the building vector dataset to obtain the final LCZ classification results (Fig. 5).

In total, there were 16 LCZs in the human settlements, i.e., LCZA, LCZC, LCZD, LCZE, LCZF, LCZG and LCZ1–10, which accounted for 4.530, 0.087, 17.975, 41.474, 0.180, 2.278, and 33.476%, of the total settlement area, respectively (Fig. 6).

3.2. Thermal environment characteristics of the LCZs

Landsat8 thermal infrared data and MODIS water vapor data (MOD), recorded at 02:35 and 02:05 (GMT) on August 9, 2018, were used to invert LST (Fig. 7) via the mono-window algorithm. To verify the effectiveness of the LST inversion, the MODIS LST product

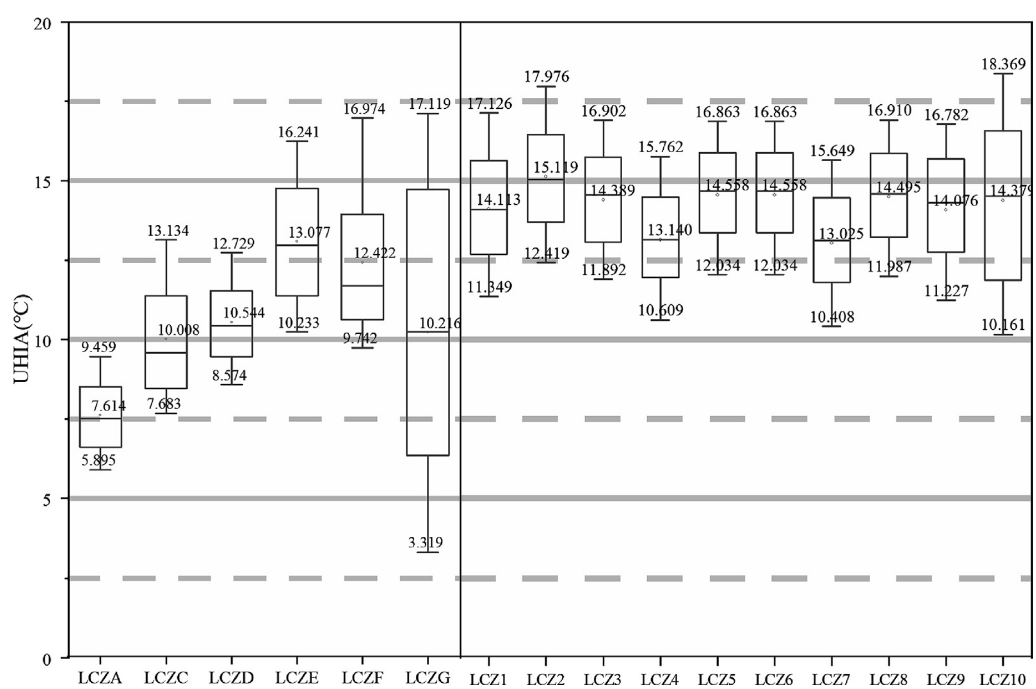

Fig. 9. The thermal environment characteristics of different LCZs.

Table 3
The total floor area and population capacity (in 30m*30m pixel area).

LCZ	Total floor area	Population capacity (person)	Per capita floor area (m^2/person)
LCZ1	≥7200 m^2	≥105	68.571
LCZ2	2700–7200 m^2	40–105	
LCZ3	0–2700 m^2	0–40	
LCZ4	≥2880 m^2	≥42	
LCZ5	1080–2880 m^2	16–42	
LCZ6	0–1080 m^2	0–16	
LCZ7	≥1440 m^2	≥21	
LCZ8	540–1440 m^2	8–21	
LCZ9	0–540 m^2	0–8	

Table 4
$UHIA_{average}$ and population capacity in LCZs (Before optimization).

LCZ	Area (km^2)	Population capacity (person)	$UHIA_{average}$ (°C)
LCZ1	3.371	346363	12.441
LCZ2	11.317	442971	
LCZ3	5.763	112788	
LCZ4	4.535	186385	
LCZ5	16.813	263238	
LCZ6	9.067	70980	
LCZ7	8.172	167931	
LCZ8	24.070	400414	
LCZ9	19.475	76229	
LCZ10	15.243	–	
LCZA	15.944	–	
LCZC	0.308	–	
LCZD	63.268	–	
LCZE	145.980	–	
LCZF	0.632	–	
LCZG	8.018	–	
Total	**351.976**	**2067300**	

Table 5
$UHIA_{average}$ and population capacity in LCZs (After optimization).

LCZ	Area (km^2)	Population capacity (person)	$UHIA_{average}$ (°C)
LCZ1	–	–	11.654
LCZ2	–	–	
LCZ3	–	–	
LCZ4	–	–	
LCZ5	28.585	508173	
LCZ6	57.170	508173	
LCZ7	57.170	1333955	
LCZ8	28.585	539934	
LCZ9	–	–	
LCZ10	–	–	
LCZA	54.236	–	
LCZC	54.236	–	
LCZD	54.236	–	
LCZE	8.959	–	
LCZF	–	–	
LCZG	8.801	–	
Total	**351.976**	**2890236**	

(MOD11L2), which was recorded at 02:25 (GMT) on August 2, 2018, was used (Fig. 8). To analyze the correlation between the Landsat LST results and MODIS11L2, the Landsat LST results were resampled to 1 km. Thus, a significant correlation was observed between the LST inverted via the mono-window algorithm using Landsat8 data and the product of the MOD11L2 LST (correlation coefficient, $R = 0.815$), indicating the reliability of the LST inversion results.

For the LCZs, A–G (A, C, D, E, F, G), the average LST values were 31.176, 32.507, 34.115, 36.681, 36.016, and 30.496 °C, respectively. LCZE and LCZG had the highest and lowest LSTs at 36.681 and 30.496 °C, respectively. For LCZ1–10, their average LST values were 37.797, 38.718, 38.002, 36.779, 38.125, 37.739, 36.688, 38.078, 37.726, and 38.102 °C, respectively. Fig. 9 shows the UHIA results for the different LCZs. For LCZA–G (A, C, D, E, F, G), the UHIA values were, 7.616, 8.947, 10.554, 13.121, 12.456, and 6.936 °C, respectively, and for LCZ1–10, they were, 14.23661, 15.158, 14.441, 13.220, 14.565, 14.183, 13.126, 14.519, 14.167, and 14.370 °C, respectively, with LCZ2 and LCZG showing the highest and lowest UHIA values at 15.158 and 7.616 °C, respectively. A comparison of the UHIA values of the LCZs at different heights showed that for compact building LCZ classes (LCZ1–3), compact mid-rise buildings (LCZ2) had the highest UHIA value, while that of compact high-rise building (LCZ1) was lowest. For open building LCZ classes (LCZ4–6), open mid-rise buildings (LCZ5) had the highest UHIA value, while that of open high-rise buildings (LCZ4) was less than that of open low-rise buildings (LCZ6). For the sparse building LCZ classes (LCZ7–9), sparse high-rise buildings (LCZ8) had a UHIA value of 14.519 °C, which was slightly higher than that of sparse low-rise buildings. A comparison of the UHIA values of the LCZs at different building densities for high-rise building (LCZ1,4,7), mid-rise building (LCZ2,5,8), or low-rise building (LCZ3,6,9) LCZs showed that the UHIA values of compact building LCZs were significantly higher than those of open and spare building LCZs. It was also observed that the UHIA values of the building LCZs were significantly higher than those corresponding to natural land cover LCZs. Additionally, the UHIA values of the compact building LCZ classes (LCZ1–3) were significantly higher than those in the open building (LCZ4–6), sparse/lightweight building (LCZ7-9), and industrial building (LCZ10) LCZs, while the UHIA values of the mid-rise building LCZs (LCZ2,5,8) were always higher than those of low-rise building and high-rise building LCZs.

3.3. *Obtaining optimal solutions*

The different LCZs had different thermal environment characteristics and population capacities. In the case of limited urban construction land and population growth, the combination of the different LCZs could reduce the negative impact of the UHI effect. A detailed evaluation of the thermal environment characteristics of the LCZs has been presented in Section 3.2. The population accommodation feature represents the number of people per unit area in the LCZs (particularly for building type LCZ1–10), and it is calculated from the building area of the LCZs and the number of permanent residents per unit area, as shown in Table 3. The LCZ population and thermal environment characteristics of the study area were as shown in Table 4.

By constructing a nonlinear solver model in LINGO, it was possible to obtain the global optimal solution (Table 5). With the current population size and human settlement area, the layout model:

LCZ5 + LCZ6 + (LCZ7+LCZ8+LCZA + LCZC + LCZD + LCZE + LCZG)

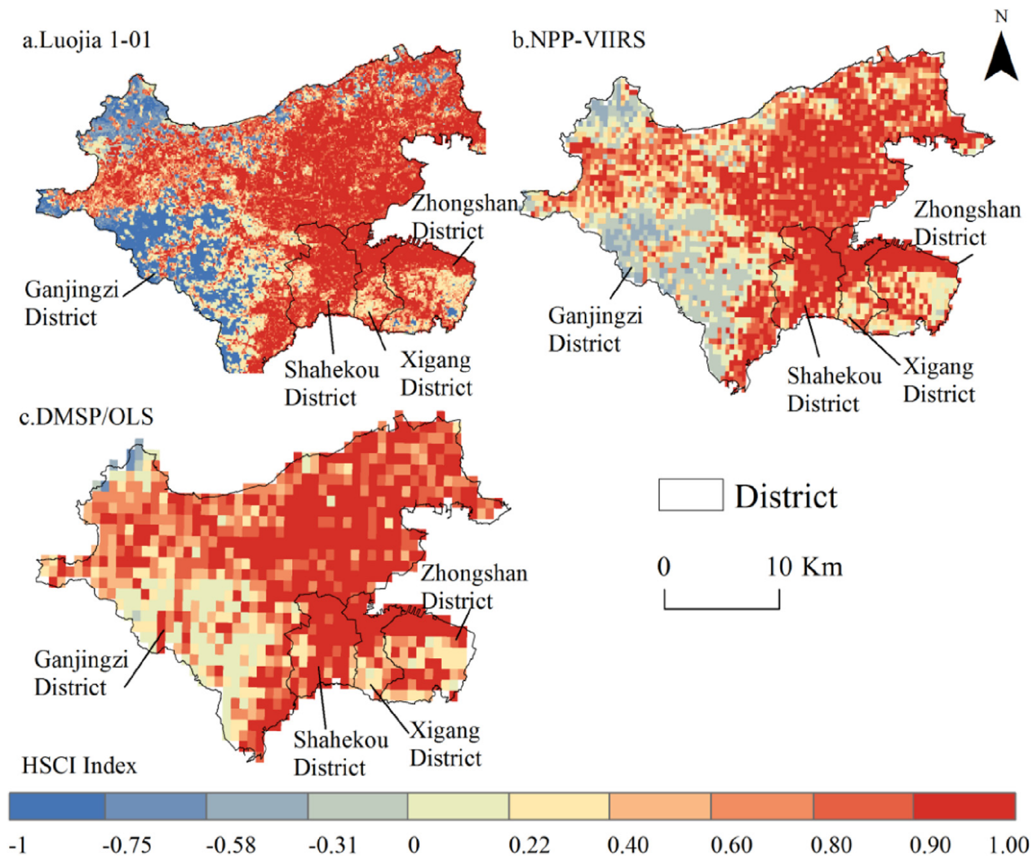

Fig. 10. HSCI index calculations based on the different nighttime lighting data.

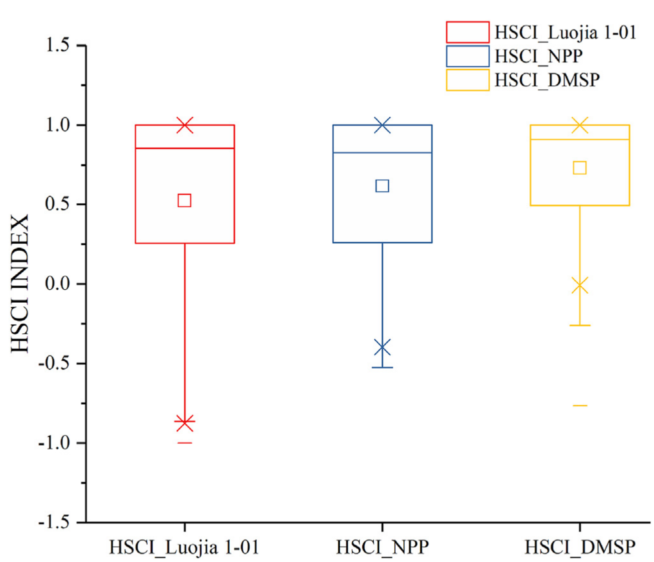

Fig. 11. HSCI index statistics based on different nighttime lighting data.

with areas 28.585, 57.170, 57.170, 28.585, 54.236, 54.236, and 54.236 km^2, respectively, which accommodated a total population of 2.890×10^6 persons, with LCZ5, LCZ6, LCZ7, and LCZ8 accommodating 508172, 508174, 1333955, and 539934 persons, respectively. This optimization process resulted in a decrease in $UHI_{Aaverage}$ values from 12.486 to 11.654 °C.

4. Discussions

4.1. Human settlements mapping

In this study, the Luojia 1-01 NTL dataset was used to calculate HSCI values, which significantly improved spatiotemporal resolution, compared with the DMSP/OLS and NPP-VIIRS datasets used in previous studies (Lu et al., 2008; Ma et al., 2018, 2015). This resulted in the enhancement of the accuracy of the extraction of the human settlements. Given that there was an offset between the Luojia1-01 images and actual objects, a preliminary geometric correction of the Luojia1-01 images was performed during data preprocessing using objects with clear features.

To visually clarify any enhancements of the HSCI calculation results, the HSCI results based on the different NTL datasets were compared, and the results (Fig. 10) showed that the HSCI values calculated based on the Luojia1-01 dataset had a superior spatial resolution, i.e., 130 m, compared with that calculated based on the DMSP/OLS and NPP-VIIRS NTL datasets. Additionally, the comparison also showed that the HSCI values calculated based on the Luojia 1-01 dataset ranged from 1.00 to −0.98 (Fig. 11), while those calculated based on the NPP-VIIRS dataset ranged from 1.00 to −0.52, and those calculated based on the DMSP/OLS dataset ranged from 1.00 to −0.87. Thus, the use of the Luojia 1-01 dataset enhanced the range of the HSCI values, making it possible to further identify urban human settlements. In summary, the calculation of HSCI using the Luojia 1-01 dataset resulted in the enhancement of the spatial resolution as well as the range of the HSCI values from the threshold.

4.2. LCZ mapping

In this study, multi-source datasets, such as remote sensing imagery and building vector datasets, were used for LCZ mapping. Compared with the LCZ mapping methods used in most previous studies, in which remote sensing images were employed to realize supervised classification, such as WUDAPT work flow (Brousse et al., 2016; R. Wang et al., 2017a; Xu et al., 2017b), the use of multi-source datasets for LCZ classification mapping provided higher classification accuracy (Gál et al., 2016). Compared with the landsat images used in previous studies, the higher resolution Sentinel-2 data used in LCZ mapping in this study significantly brought about an improvement in the spatial resolution of the LCZ classification. Additionally, when classifying LCZ10 (industrial zone), certain data were corrected based on small-scale field investigations, which further improved data reliability as well as the classification results.

4.3. UHI effect intensity calculation

In this study, UHIA is proposed as an index for the measurement of the thermal environment characteristics of LCZs. UHIA involves the calculation of the average heat island effect intensity in different LCZ ranges based on the LCZ and UHI concepts. The UHIA calculation process employed in this study is different from the original UHI calculation process, which uses the difference in the average surface temperature of different regions as the intensity of the calculation. In this study, the UHIA calculation process first involved the determination of the difference between the surface temperature and the reference temperature (the average surface temperature of LCZD). Thereafter, the average value was calculated as the intensity result of the different LCZs. The UHI intensity emphasizes the temperature difference between the different LCZs. In studies related to the remote sensing of thermal environments, the pixel is the smallest temperature observation unit. Thus, the UHI intensity could be calculated using the pixel as the basic unit, and thereafter, the characteristics of the calculation results can be statistically analyzed to reflect the thermal environment characteristics of the different LCZs. In summary, UHIA is more suitable indicator for the analysis of the heat island effect than UHI.

4.4. Obtaining optimal solutions

Previous studies on the LCZ have been primarily focused on three aspects: the construction and improvement of the LCZ classification system (Wang et al., 2016; Wang and Ouyang, 2017), LCZ mapping methods (Brousse et al., 2016; Danylo et al., 2016; R. Wang et al., 2017a), and empirical studies of the LCZ thermal environment (Beck et al., 2018; Unger et al., 2018; Verdonck et al., 2017; Y. Wang et al., 2017b; X. Yang et al., 2018a,b). Previous studies that used LCZs to study the characteristics of the thermal environment involved temperature observations (Beck et al., 2018; X. Yang et al., 2018a,b, 2017a,b) and remote sensing monitoring (Unger et al., 2018; Y. Wang et al., 2017b; J. Yang et al., 2019a). However, this study focuses on the thermal environment of LCZs and describes the use of the UHIA index to measure the differences in the thermal environmental characteristics of different LCZs. It also explores the most suitable urban LCZ layout strategy with population size and residential area as limits. Compared with previous studies on heat island effect mitigation strategies, which provided strategies solely from the perspective of thermal environment characteristics, the results of this study provide a more macroscopic and comprehensive countermeasure for heat island effect mitigation, i.e., based on the current urban human settlement and population density, these results offer the possibility to adjust the area ratio of various types of LCZs in the current city to achieve countermeasures for the alleviation of the intensity of the heat island effect. Additionally, it also provides a more scientific basis for urban environmental planning.

4.5. Limitations

This study had the following limitations. Only a single phase of data was used for analysis owing to poor data quality (cloud cover). Further, the Landsat8 TIRS dataset reflects thermal infrared features with a resolution of 100 m, which is different from the resolution of actual objects. Furthermore, the meteorological data used for calculations were derived from several meteorological stations, such that the details of the associated meteorological parameters can be improved in future studies. Additionally, the urban thermal environment is associated with a variety of influencing factors, such as the climate background, land topography, green space, and anthropocentric heat (B.J. He, 2018; He et al., 2019; Imran et al., 2018; Qi et al., 2019; Qiao et al., 2017; Sun et al., 2019; J. Yang et al., 2019b; Yue et al., 2019), which were not considered in this study. Therefore, it is necessary that future studies on the urban thermal environment should be performed using long-term high-resolution multi-source datasets (Verdonck et al., 2018).

5. Conclusions

Using the Luojia 1-01 NTL, Sentinel-2A, Landsat8, and building vector datasets, in this study, the thermal environment of different LCZs in human settlements was analyzed by constructing the cumulative index of the heat island effect intensity. Additionally, a new method for obtaining the most suitable LCZs, which have the lowest heat island effect intensity under the current urban population size and built-up area size was proposed. Based on our analysis and the results obtained, the following conclusions were arrived at.

In this study, the total human settlement area was 351.976 km^2. The Ganjingzi District had the largest human settlement area, while the Zhongshan District had the smallest. In the Shahekou and Ganjingzi Districts, 81.005 (highest) and 55.005% (lowest) of the total area was occupied by human settlements, which contained a variety of LCZ classes, including 33.476% building zones (LCZ1−10) and 66.524% natural zones (LCZA−G).

The different LCZs had different UHIA values, particularly, the LCZ2 had the largest UHIA value at 15.158 °C, while the LCZG had the smallest UHIA at 6.936 °C. The UHIA values of the building LCZs were significantly higher than those of the natural LCZs. Mid-rise building LCZs (LCZ2,5,8) had higher UHIA values than low-rise (LCZ3,6,9) and high-rise LCZs (LCZ1,4,7) buildings. Additionally, compact building LCZs (LCZ1−3) had higher UHIA values than open (LCZ4−6) and spare building LCZs (LCZ7−9).

With the current human settlements and population size, the LCZ combination with the smallest UHIA in the study area was the LCZ layout model: LCZ5 + LCZ6 + (LCZ7+LCZ8+LCZA + LCZC + LCZD + LCZE + LCZG), which had areas 28.585, 57.170, 57.170, 28.585, 54.236, 54.236, and 54.236 km^2, respectively. With the LCZ layout model, UHIA value reduce from 12.441 to 11.654 °C, indicating a decrease in the UHI of the city.

CRediT authorship contribution statement

Jun Yang: contributed to all aspects of this work. **Yichen Wang:** wrote the main manuscript text, conducted the experiment, analyzed the data. **Chunliang Xiu:** revised the paper, All authors reviewed the manuscript. **Xiangming Xiao:** revised the paper, All authors reviewed the manuscript. **Jianhong Xia:** revised the paper, All authors reviewed the manuscript. **Cui Jin:** revised the paper, All authors reviewed the manuscript.

Declaration of competing interest

The authors declare that they have no known competing financial interests or personal relationships that could have appeared to influence the work reported in this paper.

Acknowledgments

This research study was supported by the National Natural Science Foundation of China (Grant no. 41771178, 41630749) and Innovative Talents Support Program of Liaoning Province (Grant No. LR2017017). The authors would like to acknowledge all experts' contributions in the building of the model and the formulation of the strategies in this study, especially professor Wenfeng Zhan of Nanjing University.

References

Auer, A.H., 1978. Correlation of land use and cover with meteorological anomalies. J. Appl. Meteorol. 17, 636–643. https://doi.org/10.1175/1520-0450(1978)017<0636:coluac>2.0.co;2.

Bechtel, B., Pesaresi, M., See, L., Mills, G., Ching, J., Alexander, P.J., Feddema, J.J., Florczyk, A.J., Stewart, I., 2016. Towards consistent mapping of urban structures - global human settlement layer and local climate zones. Int. Arch. Photogramm. Remote Sens. Spat. Inf. Sci. - ISPRS Arch. 41, 1371–1378. https://doi.org/10.5194/isprsarchives-XLI-B8-1371-2016.

Beck, C., Straub, A., Breitner, S., Cyrys, J., Philipp, A., Rathmann, J., Schneider, A., Wolf, K., Jacobeit, J., 2018. Air temperature characteristics of local climate zones in the Augsburg urban area (Bavaria, southern Germany) under varying synoptic conditions. Urban Clim 25, 152–166. https://doi.org/10.1016/j.uclim.2018.04.007.

Brans, K.I., Engelen, J.M.T., Souffreau, C., De Meester, L., 2018. Urban hot-tubs: local urbanization has profound effects on average and extreme temperatures in ponds. Landsc. Urban Plann. 176, 22–29. https://doi.org/10.1016/j.landurbplan.2018.03.013.

Brousse, O., Martilli, A., Foley, M., Mills, G., Bechtel, B., 2016. WUDAPT, an efficient land use producing data tool for mesoscale models? Integration of urban LCZ in WRF over Madrid. Urban Clim 17, 116–134. https://doi.org/10.1016/j.uclim.2016.04.001.

Chen, D., Xu, X., Sun, Z., Liu, L., Qiao, Z., Huang, T., 2020. Assessment of Urban Heat Risk in Mountain Environments: A Case Study of Chongqing Metropolitan Area, China. Sustain. https://doi.org/10.3390/su12010309.

Danylo, O., See, L., Bechtel, B., Schepaschenko, D., Fritz, S., Gál, T., Bechtel, B., Unger, J., 2016. Contributing to WUDAPT: a local climate zone classification of two cities in Ukraine. IEEE J. Sel. Top. Appl. Earth Obs. Remote Sens. 9, 1841–1853. https://doi.org/10.1109/JSTARS.2016.2539977.

Du, H., Cai, Y., Zhou, F., Jiang, H., Jiang, W., Xu, Y., 2019. Urban blue-green space planning based on thermal environment simulation : Ecol. Indic 106, 105501. https://doi.org/10.1016/j.ecolind.2019.105501.

Fahmy, M., Ibrahim, Y., Hanafi, E., Barakat, M., 2018. Would LEED-UHI greenery and high albedo strategies mitigate climate change at neighborhood scale in Cairo, Egypt? Build. Simul. https://doi.org/10.1007/s12273-018-0463-7.

Gál, T., Bechtel, B., Unger, J., 2015. Comparison of two different Local Climate Zone mapping methods. ICUC9, Toulouse, Fr 9, 1–6. https://doi.org/10.1109/JSTARS.2016.2539977, 20-24 July.

Gál, T., Bechtel, B., Unger, J., 2016. Comparison of two different Local Climate Zone mapping methods. IEEE J. Sel. Top. Appl. Earth Obs. Remote Sens. 9, 1841–1853. https://doi.org/10.1109/JSTARS.2016.2539977.

Geletič, J., Lehnert, M., Savić, S., Milošević, D., 2018. Modelled spatiotemporal variability of outdoor thermal comfort in local climate zones of the city of Brno, Czech Republic. Sci. Total Environ. 624, 385–395. https://doi.org/10.1016/j.scitotenv.2017.12.076.

Golnoosh, Manteghi, Mostofa, T., 2020. Evaporative pavements as an urban heat island (uhi) mitigation Strategy : a review. Int. Trans. J. Eng. Manag. Appl. Sci. Technol. https://doi.org/10.14456/ITJEMAST.2020.17.

He, Bao-Jie, 2018. Potentials of meteorological characteristics and synoptic conditions to mitigate urban heat island effects. Urban Clim 24, 26–33. https://doi.org/10.1016/j.uclim.2018.01.004.

He, B.J., 2018. Potentials of meteorological characteristics and synoptic conditions to mitigate urban heat island effects. Urban Clim 24, 26–33. https://doi.org/10.1016/j.uclim.2018.01.004.

He, S., Zhang, Y., Zhang, J., 2018. Urban local climate zone mapping and apply in urban environment study. IOP Conf. Ser. Earth Environ. Sci. 113 https://doi.org/10.1088/1755-1315/113/1/012055.

He, B.J., Ding, L., Prasad, D., 2019. Enhancing urban ventilation performance through the development of precinct ventilation zones: a case study based on the Greater Sydney, Australia. Sustain. Cities Soc. 47, 101472 https://doi.org/10.1016/j.scs.2019.101472.

Imran, H.M., Kala, J., Ng, A.W.M., Muthukumaran, S., 2018. Effectiveness of green and cool roofs in mitigating urban heat island effects during a heatwave event in the city of Melbourne in southeast Australia. J. Clean. Prod. https://doi.org/10.1016/j.jclepro.2018.06.179.

Jhaldiyal, A., Gupta, K., Gupta, P.K., Thakur, P., Kumar, P., 2018. Urban Morphology Extractor: a spatial tool for characterizing urban morphology. Urban Clim 24, 237–246.

Jiang, W., He, G., Long, T., Guo, H., Yin, R., Leng, W., Liu, H., Wang, G., 2018. Potentiality of using luojia 1-01 nighttime light imagery to investigate artificial light pollution. Sensors 18. https://doi.org/10.3390/s18092900.

Jochem, W.C., Bird, T.J., Tatem, A.J., 2018. Identifying residential neighbourhood types from settlement points in a machine learning approach. Comput. Environ. Urban Syst. 69, 104–113. https://doi.org/10.1016/j.compenvurbsys.2018.01.004.

Kotharkar, R., Bagade, A., 2018. Local Climate Zone classification for Indian cities: a case study of Nagpur. Urban Clim 24, 369–392. https://doi.org/10.1016/j.uclim.2017.03.003.

Li, S., Chen, X., 2014. A new bare-soil index for rapid mapping developing areas using landsat 8 data, in: International Archives of the Photogrammetry, Remote Sensing and Spatial Information Sciences - ISPRS Archives. https://doi.org/10.5194/isprsarchives-XL-4-139-2014.

Li, H., Zhou, Y., Wang, X., Zhou, X., Zhang, H., Sodoudi, S., 2019. Quantifying urban heat island intensity and its physical mechanism using WRF/. UCM. Sci. Total Environ. 650, 3110–3119. https://doi.org/10.1016/j.scitotenv.2018.10.025.

Lu, D., Tian, H., Zhou, G., Ge, H., 2008. Regional mapping of human settlements in southeastern China with multisensor remotely sensed data. Remote Sens. Environ. 112, 3668–3679. https://doi.org/10.1016/j.rse.2008.05.009.

Ma, T., Zhou, Y., Zhou, C., Haynie, S., Pei, T., Xu, T., 2015. Night-time light derived estimation of spatio-temporal characteristics of urbanization dynamics using DMSP/OLS satellite data. Remote Sens. Environ. 158, 453–464. https://doi.org/10.1016/j.rse.2014.11.022.

Ma, T., Xu, T., Huang, L., Zhou, A., 2018. Human settlement composite index (HSCI) derived from nighttime luminosity associated with imperviousness and vegetation indexes. Rem. Sens. 10 https://doi.org/10.3390/rs10030455.

Maly, M.T., 2000. The neighborhood diversity index: a complementary measure of racial residential settlement. J. Urban Aff. 22, 37–47. https://doi.org/10.1111/0735-2166.00038.

Mitchell, D., James, R., Forster, P.M., Betts, R.A., Shiogama, H., Allen, M., 2016. Realizing the impacts of a 1.5 °C warmer world. Nat. Clim. Change 6, 735–737. https://doi.org/10.1038/nclimate3055.

Oke, T.R., 1976. The distinction between canopy and boundary-layer urban heat Islands. Atmosphere 14, 268–277. https://doi.org/10.1080/00046973.1976.9648422.

Perera, N.G.R., Emmanuel, R., 2018. A "Local Climate Zone" based approach to urban planning in Colombo, Sri Lanka. Urban Clim 23, 188–203. https://doi.org/10.1016/j.uclim.2016.11.006.

Qi, J. Da, He, B.J., Wang, M., Zhu, J., Fu, W.C., 2019. Do grey infrastructures always elevate urban temperature? No, utilizing grey infrastructures to mitigate urban heat island effects. Sustain. Cities Soc. 46, 101392 https://doi.org/10.1016/j.scs.2018.12.020.

Qiao, Z., Xu, X., Wu, F., Luo, W., Wang, F., Liu, L., Sun, Z., 2017. Urban ventilation network model: a case study of the core zone of capital function in Beijing metropolitan area. J. Clean. Prod. 168, 526–535.

Qin, Z., Karnieli, A., Berliner, P., 2001. A mono-window algorithm for retrieving land surface temperature from Landsat TM. Int. J. Rem. Sens. 22, 3719–3746. https://doi.org/10.1080/01431160010006971.

Quan, S.J., Dutt, F., Woodworth, E., Yamagata, Y., Yang, P.P.J., 2017. Local climate zone mapping for energy resilience: a fine-grained and 3D approach. Energy Procedia 105, 3777–3783. https://doi.org/10.1016/j.egypro.2017.03.883.

Rizwan, A.M., Dennis, L.Y.C., Liu, C., Memon, R.A., Leung, D.Y., Chunho, L., 2008. A review on the generation, determination and mitigation of Urban Heat Island. J. Environ. Sci. 20, 120–128. https://doi.org/10.1016/S1001-0742(08)60019-4.

Shi, Y., Lau, K.K.L., Ren, C., Ng, E., 2018. Evaluating the local climate zone classification in high-density heterogeneous urban environment using mobile measurement. Urban Clim 25, 167–186. https://doi.org/10.1016/j.uclim.2018.07.001.

Stewart, I.D., Oke, T.R., 2012. Local climate zones for urban temperature studies. Bull. Am. Meteorol. Soc. 93, 1879–1900. https://doi.org/10.1175/BAMS-D-11-00019.1.

Stewart, I.D., Oke, T.R., Krayenhoff, E.S., 2014. Evaluation of the "local climate zone" scheme using temperature observations and model simulations. Int. J. Climatol. 34, 1062–1080. https://doi.org/10.1002/joc.3746.

Sun, R., Lü, Y., Yang, X., Chen, L., 2019. Understanding the variability of urban heat islands from local background climate and urbanization. J. Clean. Prod. https://doi.org/10.1016/j.jclepro.2018.10.178.

Tong, Z., Chen, Y., Malkawi, A., 2017. Estimating natural ventilation potential for high-rise buildings considering boundary layer meteorology. Appl. Energy 193, 276–286. https://doi.org/10.1016/j.apenergy.2017.02.041.

Tu, L., Qin, Z., Li, W., Geng, J., Yang, L., Zhao, S., Zhan, W., Wang, F., 2016. Surface urban heat island effect and its relationship with urban expansion in Nanjing, China. J. Appl. Remote Sens. 10, 026037 https://doi.org/10.1117/1.JRS.10.026037.

Unger, J., Lelovics, E., Gál, T., 2014. Local climate zone mapping using GIS methods in Szeged. Hungarian Geogr. Bull. 63, 29–41. https://doi.org/10.15201/

hungeobull.63.1.3.
Unger, J., Skarbit, N., Gál, T., 2018. Evaluation of outdoor human thermal sensation of local climate zones based on long-term database. Int. J. Biometeorol. 62, 183–193. https://doi.org/10.1007/s00484-017-1440-z.
Verdonck, M.L., Van Coillie, F., De Wulf, R., Okujeni, A., Van Der Linden, S., Demuzere, M., Hooyberghs, H., 2017. Thermal evaluation of the local climate zone scheme in Belgium. 2017 Jt. Urban Remote Sens. Event, JURSE 2017 7–10. https://doi.org/10.1109/JURSE.2017.7924556.
Verdonck, M.L., Demuzere, M., Hooyberghs, H., Beck, C., Cyrys, J., Schneider, A., Dewulf, R., Van Coillie, F., 2018. The potential of local climate zones maps as a heat stress assessment tool, supported by simulated air temperature data. Landsc. Urban Plann. 178, 183–197. https://doi.org/10.1016/j.landurbplan.2018.06.004.
Voogt, J.A., Oke, T.R., 2003. Thermal remote sensing of urban climates. Remote Sens. Environ. 86, 370–384. https://doi.org/10.1016/S0034-4257(03)00079-8.
Wang, J., Ouyang, W., 2017. Attenuating the surface urban heat island within the local thermal zones through land surface modification. J. Environ. Manag. 187, 239–252. https://doi.org/10.1016/j.jenvman.2016.11.059.
Wang, F., Qin, Z., Song, C., Tu, L., Karnieli, A., Zhao, S., 2015a. An improved mono-window algorithm for land surface temperature retrieval from landsat 8 thermal infrared sensor data. Rem. Sens. 7, 4268–4289. https://doi.org/10.3390/rs70404268.
Wang, J., Qingming, Z., Guo, H., Jin, Z., 2015b. Characterizing the spatial dynamics of land surface temperature–impervious surface fraction relationship. Int. J. Appl. Earth Obs. Geoinf. 45, 55–65. https://doi.org/10.1016/j.jag.2015.11.006.
Wang, J., Qingming, Z., Guo, H., Jin, Z., 2016. Characterizing the spatial dynamics of land surface temperature–impervious surface fraction relationship. Int. J. Appl. Earth Obs. Geoinf. 45, 55–65. https://doi.org/10.1016/j.jag.2015.11.006.
Wang, R., Ren, C., Xu, Y., Lau, K.L.K.K.-L., Shi, Y., 2017. Mapping the local climate zones of urban areas by GIS-based and WUDAPT methods: a case study of Hong Kong. Urban Clim. https://doi.org/10.1016/j.uclim.2017.10.001.
Wang, Y., Zhan, Q., Ouyang, W., 2017b. Impact of urban climate landscape patterns on land surface temperature in wuhan, China. Sustainability 9, 1700. https://doi.org/10.3390/su9101700.
Wong, M.S., Nichol, J.E., To, P.H., Wang, J., 2010. A simple method for designation of urban ventilation corridors and its application to urban heat island analysis. Build. Environ. 45, 1880–1889. https://doi.org/10.1016/j.buildenv.2010.02.019.
Wu, H.J., Yuan, Z.W., Zhang, L., Bi, J., 2012. Life cycle energy consumption and CO2 emission of an office building in China. Int. J. Life Cycle Assess. https://doi.org/10.1007/s11367-011-0342-2.
Xu, H., 2006. Modification of normalised difference water index (NDWI) to enhance open water features in remotely sensed imagery. Int. J. Rem. Sens. https://doi.org/10.1080/01431160600589179.
Xu, H., 2013. Analysis of impervious surface and its impact on urban heat environment using the normalized difference impervious surface index (NDISI). Photogramm. Eng. Rem. Sens. https://doi.org/10.14358/pers.76.5.557.
Xu, Y., Ren, C., Cai, M., Yan, N., Edward, Y., Wu, T., 2017a. Classification of local climate zones using ASTER and landsat data for high-density cities. IEEE J. Sel. Top. Appl. Earth Obs. Remote Sens. 10, 3397–3405. https://doi.org/10.1109/JSTARS.2017.2683484.
Xu, Y., Ren, C., Ma, P., Ho, J., Wang, W., Lau, K.K., Lin, H., Ng, E., 2017b. Urban morphology detection and computation for urban climate research. Landsc. Urban Plann. 167, 212–224. https://doi.org/10.1016/j.landurbplan.2017.06.018.
Yan, H., Wu, F., Dong, L., 2018. Influence of a large urban park on the local urban thermal environment. Sci. Total Environ. 622 (623), 882–891. https://doi.org/10.1016/j.scitotenv.2017.11.327.
Yang, X., Yue, W., Xu, H., Wu, J., He, Y., 2014. Environmental consequences of rapid urbanization in Zhejiang province, East China. Int. J. Environ. Res. Publ. Health 11, 7045–7059. https://doi.org/10.3390/ijerph110707045.
Yang, J., Sun, J., Ge, Q., Li, X., 2017a. Assessing the impacts of urbanization-associated green space on urban land surface temperature: a case study of Dalian. China. Urban For. Urban Green. 22, 1–10. https://doi.org/10.1016/j.ufug.2017.01.002.
Yang, X., Yao, L., Zhu, C., Jin, T., Peng, L.L., 2017b. Analysis of local heat islands in nanjing, China, based on the local climate zone scheme. Procedia Eng 205, 2501–2508. https://doi.org/10.1016/j.proeng.2017.09.980.
Yang, J., Su, J., Xia, J.C., Jin, C., Li, X., Ge, Q., 2018a. The impact of spatial form of urban architecture on the urban thermal Environment : a case study of the zhongshan district, dalian, China. IEEE J. Sel. Top. Appl. Earth Obs. Remote Sens. 99, 1–8.
Yang, X., Yao, L., Jin, T., Peng, L.L.H., Jiang, Z., Hu, Z., Ye, Y., 2018b. Assessing the thermal behavior of different local climate zones in the Nanjing metropolis, China. Build. Environ. Times 137, 171–184. https://doi.org/10.1016/j.buildenv.2018.04.009.
Yang, X., Ye, T., Zhao, N., Chen, Q., Yue, W., Qi, J., Zeng, B., Jia, P., 2019. Population mapping with multisensor remote sensing images and point-of-interest data. Rem. Sens. 11, 574. https://doi.org/10.3390/rs11050574.
Yang, J., Jin, S., Xiao, X., Jin, C., Xia, J., Cecilia), Li, X., Wang, S., 2019a. Local climate zone ventilation and urban land surface temperatures: towards a performance-based and wind-sensitive planning proposal in megacities. Sustain. Cities Soc. 47, 1–11. https://doi.org/10.1016/j.scs.2019.101487.
Yang, J., Wang, Y., Xiao, X., Jin, C., Xia, J., Cecilia), Li, X., 2019b. Spatial differentiation of urban wind and thermal environment in different grid sizes. Urban Clim 28, 100458. https://doi.org/10.1016/j.uclim.2019.100458.
Yang, X., Peng, L.L.H., Jiang, Z., Chen, Y., Yao, L., He, Y., 2020. Impact of urban heat island on energy demand in buildings : local climate zones in Nanjing. Appl. Energy 260, 114279. https://doi.org/10.1016/j.apenergy.2019.114279.
Yao, R., Wang, L., Huang, X., Zhang, W., Li, J., Niu, Z., 2018. Interannual variations in surface urban heat island intensity and associated drivers in China. J. Environ. Manag. 222, 86–94. https://doi.org/10.1016/j.jenvman.2018.05.024.
Ye, T., Zhao, N., Yang, X., Ouyang, Z., Liu, X., Chen, Q., Hu, K., Yue, W., Qi, J., Li, Z., Jia, P., 2019. Improved population mapping for China using remotely sensed and points-of-interest data within a random forests model. Sci. Total Environ. 658, 936–946. https://doi.org/10.1016/j.scitotenv.2018.12.276.
Yin, C., Yuan, M., Lu, Y., Huang, Y., Liu, Y., 2018. Effects of urban form on the urban heat island effect based on spatial regression model. Sci. Total Environ. 634, 696–704. https://doi.org/10.1016/j.scitotenv.2018.03.350.
Yue, W., Liu, X., Zhou, Y., Liu, Y., 2019. Impacts of urban configuration on urban heat island: an empirical study in China mega-cities. Sci. Total Environ. 671, 1036–1046. https://doi.org/10.1016/j.scitotenv.2019.03.421.
Zhan, W., Ju, W., Hai, S., Ferguson, G., Quan, J., Tang, C., Guo, Z., Kong, F., 2014. Satellite-derived subsurface urban heat island. Environ. Sci. Technol. 48, 12134–12140. https://doi.org/10.1021/es5021185.
Zhang, B., Bi, J., Yuan, Z., Ge, J., 2007. Who will be more active in sustainable consumption? Evidence from China. Int. J. Environ. Sustain Dev. https://doi.org/10.1504/IJESD.2007.016242.
Zheng, Y., Ren, C., Shi, Y., Lau, K.K.-L., Yim, S.H.L., Lai, D.Y.F., Ho, J., Ng, E., 2015. Applying " local climate zone (LCZ)" into a high-density high-rise cities - a pilot study in Hong Kong. ICUC9, Toulouse, Fr 1–6, 20-24 July.
Zheng, Y., Ren, C., Xu, Y., Wang, R., Ho, J., Lau, K., Ng, E., 2018. GIS-based mapping of Local Climate Zone in the high-density city of Hong Kong. Urban Clim 24, 419–448. https://doi.org/10.1016/j.uclim.2017.05.008.
Zhou, D., Zhang, L., Li, D., Huang, D., Zhu, C., 2016. Climate-vegetation control on the diurnal and seasonal variations of surface urban heat islands in China. Environ. Res. Lett. 11 https://doi.org/10.1088/1748-9326/11/7/074009.